Spatial Domain Interactions between Ultraweak Optical Beams

Utsab Khadka,[1,*,‡] Jiteng Sheng,[1] and Min Xiao[1,2,†]

[1]*Department of Physics, University of Arkansas, Fayetteville, Arkansas 72701, USA*

[2]*Department of Physics and National Laboratory of Solid State Microstructures, Nanjing University, Nanjing 210093, China*

(Received 4 January 2013; published 26 November 2013)

We have observed spatial interactions between two ultraweak optical beams that are initially collinear and nonoverlapping. The weak beams are steered towards each other by a spatially varying cross-Kerr refractive index waveguide written by a strong laser beam in a three-level coherently prepared atomic medium. After fusing together, the combined beam shows controllable phase-dependent behaviors. This is the first observation of solitonlike interactions between weak beams and can be useful for all-optically tunable beam combining, switching, and gating for weak photonic signals.

DOI: 10.1103/PhysRevLett.111.223601 PACS numbers: 42.50.Gy, 42.65.Tg, 42.79.Ta

It is well known that two optical fields that are spatially apart can interact with each other in a nonlinear optical medium, and that the interaction can be tuned via the relative phase between the fields [1–9]. Such a phase-dependent effect has been demonstrated commonly in soliton collision experiments where, depending on the relative phase between the solitons, different outcomes are achieved such as fusion and repulsion. These experimental observations were made in photorefractive crystals as well as in atomic vapors, which have different (quadratic and cubic) nonlinearities, respectively. In those experimental demonstrations, the solitons are achieved when the laser beams self-waveguide themselves due to self-focusing [10–12], which is a nonlinear effect arising due to an intensity-dependent refractive index $n(I)$. The conditions for stability of solitons of different dimensions have been extensively investigated [13,14]. The self-induced nonlinearities require the beams to have large intensities, so typically high-powered pulses with narrow temporal and spatial widths are used. In the two-soliton interaction case, the interference between the two fields causes the intensity in the overlapping region to vary with their relative phase difference. For instance, in the in-phase case, constructive interference enhances the intensity and the nonlinear refractive index in this region, thus steering both solitons to this region and resulting in their fusion. Such phase-dependent interactions for two self-waveguiding beams can be important in constructing all-optical gates and switches for optical signals, as shown in Fig. 1(a). Here, we ask the question: can similar spatial-domain interactions be induced between two beams having very weak intensities and insignificant self-induced nonlinearities? Such interactions will be important ingredients in communication and computation protocols for weak photonic signals. Recently, theoretical studies have predicted the generation of stable ultraweak intensity solitons and their collisions in three- and four-level systems [15–22], where the all-optical wave guiding is achieved via quantum coherence effects induced by additional strong coupling beams.

In this Letter, we experimentally demonstrate the phase-dependent interactions between two initially spatially separated optical fields having very weak intensities. Here, a spatially varying cross-Kerr refractive index profile for the weak beams is induced by a strong coupling beam that is partially overlapped with both of the weak signal beams initially inside a vapor cell containing three-level rubidium atoms, which generates a common, tunable all-optical waveguide utilizing quantum coherence. In this way, by utilizing the large cross-Kerr effect, we relax the requirement for the two signal fields themselves to have large intensities in order to achieve the needed spatial refractive index gradient.

The experimental setup and the relevant atomic system are shown in Fig. 1. Two weak probe beams $\mathbf{E_1}$ and $\mathbf{E_1'}$ are derived from the same diode laser. The output of the diode laser is first fed into a single-mode polarization maintaining fiber (not shown in figure) for mode cleaning. The strong

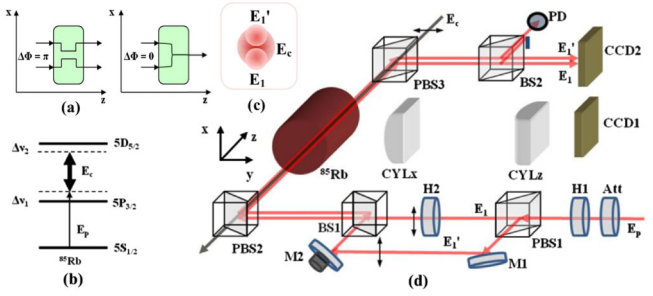

FIG. 1 (color online). (a) Schematic diagram of phase-dependent spatial interactions between two optical fields inside a nonlinear optical medium (green shaded region). (b) Atomic system. (c) Beam overlap geometry. (d) Simplified experimental setup. Att = variable neutral-density attenuator wheel, (P)BS = (polarizing) beam splitting cube, H = half-wave plate, CYL = cylindrical lens, CCD = charge-coupled device camera, PD = fast photodiode, M = mirror.

coupling beam $\mathbf{E}_c$ is from a Ti:sapphire ring laser. All three beams are continuous wave (cw), nearly collimated, and have Gaussian spatial profiles. Beams $\mathbf{E_1}$ and $\mathbf{E_1'}$ are nearly collinear with a vertical separation between their centroids and negligible overlap. The beam $\mathbf{E}_c$ counterpropagates with $\mathbf{E_1}$ and $\mathbf{E_1'}$, such that $\mathbf{E}_c$'s centroid is in the middle of the centroids of $\mathbf{E_1}$ and $\mathbf{E_1'}$, and $\mathbf{E}_c$ overlaps partially with both $\mathbf{E_1}$ and $\mathbf{E_1'}$ [Fig. 1(c)]. $\mathbf{E_1}$ and $\mathbf{E_1'}$ are linearly polarized in the plane containing them, while $\mathbf{E}_c$ has a linear polarization orthogonal to $\mathbf{E_1}$ and $\mathbf{E_1'}$. The strengths of $\mathbf{E_1}$ and $\mathbf{E_1'}$ can be controlled independently by the half-wave plates and polarization beam splitters, and together by the neutral density attenuator wheel. One of the mirrors ($M2$) in the path of $\mathbf{E_1'}$ is piezo-actuated, allowing control of the relative phase $\Delta\Phi_1$ between $\mathbf{E_1}$ and $\mathbf{E_1'}$. Another mirror on $\mathbf{E_1'}$s path (not shown in the figure) is placed on a micrometer translational stage, such that the separation between the fields can be easily tuned.

The average width of the coupling beam inside the vapor cell is $w_c = 156\ \mu$m. The widths of the probe beams at the entrance of the vapor cell are $w_1 = 133\ \mu$m and $w_1' = 148\ \mu$m, and the distance between their centers is 120 μm. When propagating in free space, these beams slowly diverge and by the time they travel 325 mm to the charge coupled device camera CCD2, where they are imaged without using a lens, their widths are $w_1 = 670\ \mu$m and $w_1' = 600\ \mu$m. In order to prevent the overlap of these probe beams at CCD2, they are aligned with a small angle between them so that at CCD2, the separation between their centers is larger than their widths.

The three fields pass through a Rb vapor cell that is heated to 95 °C by a heating coil. The vapor cell is 7.5 cm long, and 3.5 cm of the cell's central portion is accessible for fluorescence imaging. The fields $\mathbf{E_1}$ and $\mathbf{E_1'}$ are nearly resonant with the D_2 transition ($\sim$780.23 nm). They have a frequency detuning of $\Delta\nu_1 = 400$ MHz towards the blue side of the $F = 3 \rightarrow F' = 4$ transition of the ^{85}Rb isotope. The coupling beam E_c drives the $5P_{3/2} \rightarrow 5D_{5/2}$ transition ($\sim$775.98 nm), and its frequency detuning $\Delta\nu_2$ can be tuned in 10 MHz increments. The transverse spatial profiles (x-y dimension) of the transmitted probe beams are imaged at CCD2, which is 25 cm away from the Rb cell's exit. The counterpropagating beam geometry effectively isolates the strong coupling beam from the weak probe beams before they reach CCD2 with minimal background noises. The transmitted field $\mathbf{E_1}$ is also monitored by a photodiode for spectral characterization.

The camera CCD1 takes images of the x-z dimension of the beams inside the vapor cell via fluorescence from the side of the Rb cell. The fluorescence is imaged onto CCD1 by two cylindrical lenses CYLx and CYLz with focal lengths 10 cm each, which are positioned such that the x and z dimensions are magnified by factors of 4 and 1/4 at CCD1, respectively. This way, a significant axial length of the beams within the vapor cell (almost 25 mm) can be imaged while still maintaining a good resolution over a range of 1 mm of the transverse (x) dimension at the CCD plane. CYLx, CYLz, and CCD1 are each placed in three-dimensional micrometer-precision stages with translational and rotational degrees of freedom to facilitate the imaging process. Furthermore, the beams $\mathbf{E_1}$ and $\mathbf{E_1'}$ are linearly polarized in the x-z plane so as to maximize the dipole-scattered radiation pattern at CCD1.

In the three-level ladder-type atomic medium, a strong coupling beam alters the absorption and dispersion of a weak probe beam via quantum coherence. The close frequency of the two subsequent transitions in the ladder scheme and the counterpropagating geometry of the beams results in essential suppression of Doppler broadening at the two-photon transition compared to one-photon transition. When both one-photon and two-photon resonances are met, the atomic medium is rendered transparent for the probe beam by virtue of electromagnetically induced transparency (EIT). Within the spectral window of EIT, the transmission of the probe beam increases, and it also experiences a rapidly varying refractive index [23,24]. The value of the refractive index can be controlled by the coupling beam's intensity I_c and the two-photon detuning. The dependence of the susceptibility on Ω_c^2, where Ω_c is the coupling beam's Rabi frequency, and the Gaussian spatial distribution of $\Omega_c(\mathbf{r})$, means that the weak probe beam experiences a spatially varying refractive index $n(\mathbf{r})$ which can give rise to lensing and waveguiding behaviors. Such cross-Kerr induced focusing and defocusing for perfectly overlapped probe and coupling beams in the ladder-type configuration with counterpropagating geometry was reported in Ref. [25].

In our setup the coupling beam $\mathbf{E}_c$, which is on the order of 10^5 more intense than the probe beams, has a rapidly varying transverse spatial profile. The probe beams are placed at the opposite sides of this Gaussian intensity distribution. In order to find the correct profile for $n(\mathbf{r})$ that yields stable waveguiding for the weak probe beams along the axis of the coupling beam, the correct combination of parameters (I_c, $\Delta\nu_1$, $\Delta\nu_2$, cell temperature,...) has to be found. We explored the large parameter space both experimentally and numerically and found that the correct shape of $n(\mathbf{r})$ supporting waveguiding, as well as the stability of the waveguided beams, is very sensitive to the parameters and initial geometrical conditions.

Numerically calculated transverse refractive index profiles for various parameters are shown in Fig. 2(a). To obtain these results, the density-matrix equations for the three-level system are solved, and then numerically integrated over all the atomic velocities to account for Doppler broadening. It is clear that only certain parameters will yield the proper index profiles that support confinement of the weak beams. The parameters giving rise to the refractive index profile in Fig. 2(a) (iii), which are similar to the ones used in the experiment, are used in tracing the trajectories of the

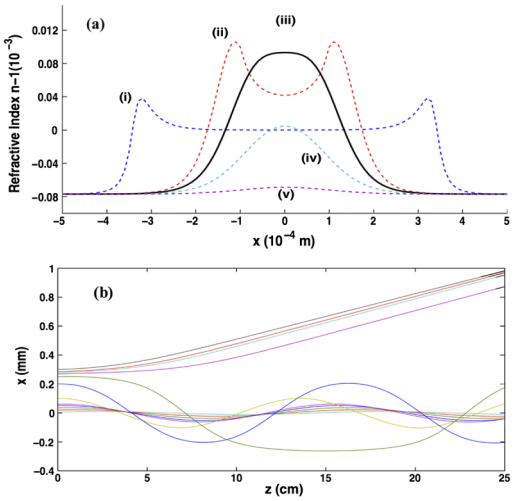

FIG. 2 (color online). Numerical calculations: (a) Transverse refractive index for $\Delta\nu_1 = +300$ MHz, $\Omega_c = 250$ MHz, $w_c = 156$ μm, (i) $\Delta\nu_2 = 0$ MHz; (ii) $\Delta\nu_2 = +15$ MHz; (iii) $\Delta\nu_2 = +25$ MHz; (iv) $\Delta\nu_2 = +50$ MHz; (v) $\Delta\nu_2 = +250$ MHz. (b) Probe beam trajectories for different initial transverse positions $x_0 = [5, 20, 35, 50, 60, 100, 200, 250, 270, 280, 285, 300]$ μm with the transverse refractive index profile of (a)(iii).

probe beam $\mathbf{E}_1'$ for different initial conditions [Fig. 2(b)]. The trajectories are found by extremizing the time taken by the rays to traverse through the medium, i.e., by using Fermat's principle. The probe beam is waveguided for only a small range of initial transverse position x_0 and angle θ_0 with respect to the coupling beam's axis. Figure 2(b) shows numerical solutions demonstrating some values of x_0 leading to waveguiding, as well as some that do not support the waveguiding. Here, various trajectories of one probe beam are traced, whereas the other beam's trajectories show similar dependences on the parameters and initial conditions. The waveguiding occurs for only a small range of initial launch angle θ_0.

Once the two weak fields (~ 400 nW each) are steered inside this common all-optical waveguide, the interaction between them becomes dependent on their relative phase difference $\Delta\Phi_1$. When $\Delta\Phi_1 = 0$, the intensity in the central region of the waveguide becomes maximum [Fig. 3(b)]. For $\Delta\Phi_1 = \pi$, the two fields interfere destructively and the central region of the waveguide remains dark [Fig. 3(c)]. This is equivalent to the interaction of Fig. 1(a), which was previously demonstrated between two strong self-guided beams, and now demonstrated between two ultraweak beams by making use of quantum coherence. Furthermore, the output state in the current case has more tunability. For the in-phase case [Fig. 3(b)], the output intensity of the central bright component can be all-optically tuned via the intensity of the coupling beam [Fig. 3(d)]. This is because in this system we not only modify the refractive index, but also the transparency of the medium itself. In the previous demonstrations of two-beam fusion using self-induced nonlinearities, the output intensity cannot be tuned since the fusion is critically dependent on both the relative phase and the signal beam

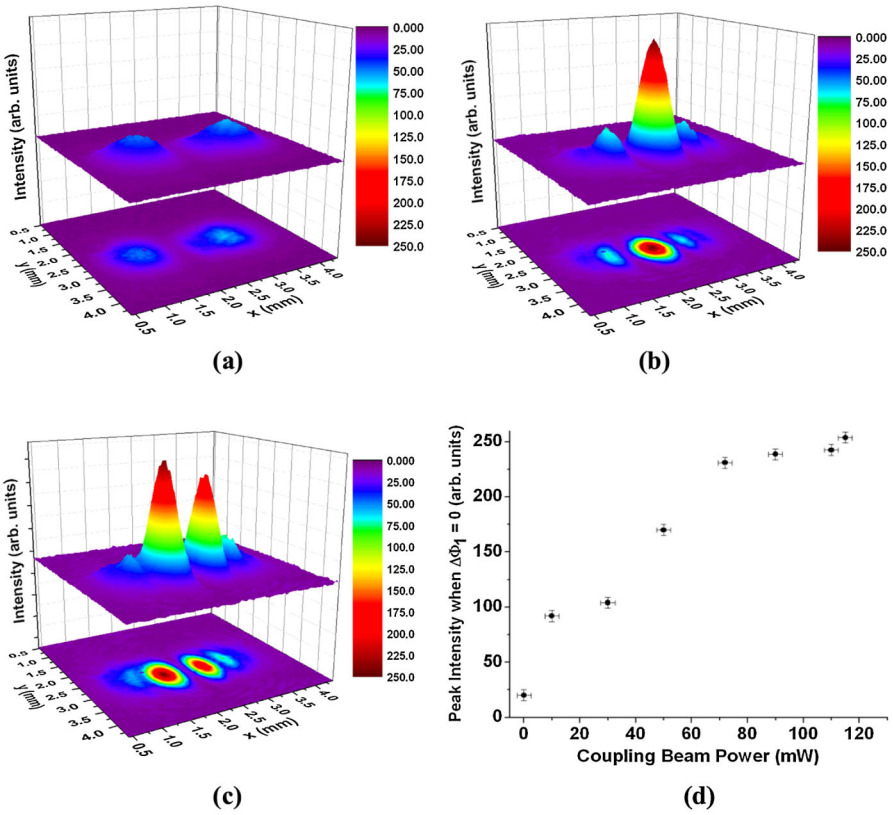

FIG. 3 (color online). Two-dimensional transverse images taken by CCD2 when the two-photon detuning is nearly on resonance. Cell temperature = 95 °C, $\Delta\nu_1 = +300$ MHz, $\Delta\nu_2 = +10$ MHz. Beam powers are measured before Rb cell. $P_1 = P_1' = 400$ nW. (a) $P_2 = 0$ mW, (b) $P_2 = 115$ mW, $\Delta\Phi_1 = 0$, (c) $P_2 = 115$ mW, $\Delta\Phi_1 = \pi$. (d) The in-phase condition similar to (b) is used, and the peak intensity of the central fused component is measured as a function of the coupling beam power P_2.

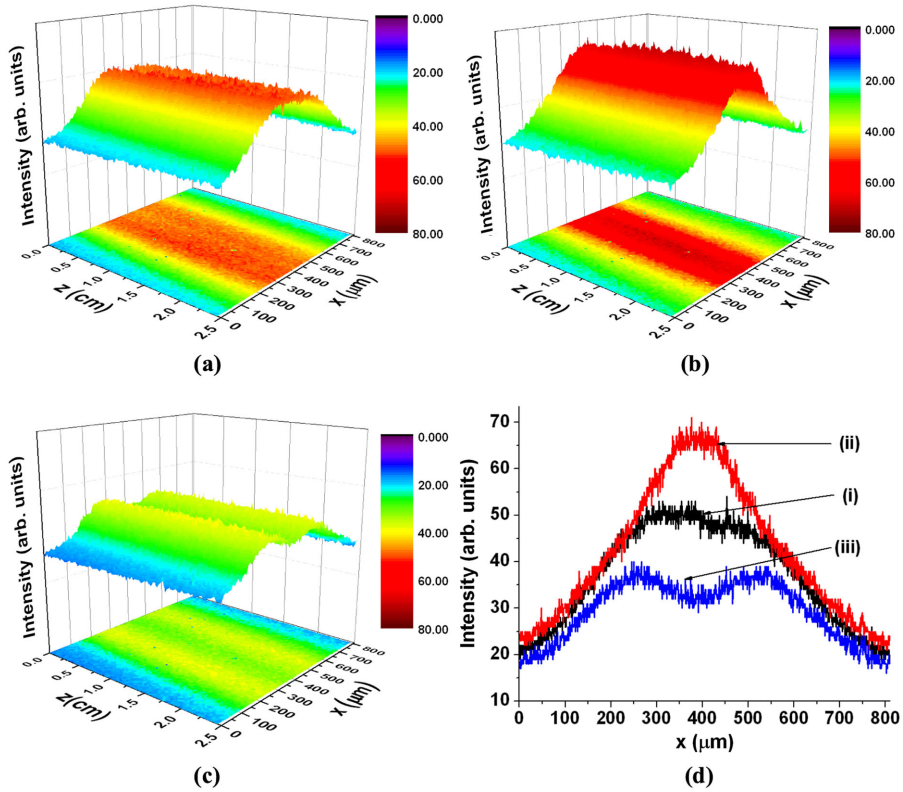

FIG. 4 (color online). Longitudinal images taken by CCD1 when the two-photon detuning is off-resonance. Cell temperature = 95 °C, $\Delta\nu_1 = +400$ MHz. Beam powers are measured before Rb cell with $P1 = P1' = 400\ \mu$W. Note the different scales of the axes: x is in μm, but z in cm, achieved by the specially designed imaging system. (a) $P_2 = 0$ mW; (b) $P_2 = 90$ mW, $\Delta\nu_2 = +250$ MHz, attractive; (c) $P_2 = 90$ mW, $\Delta\nu_2 = -250$ MHz, repulsive. (d) Curves (i), (ii), and (iii) are the one-dimensional cross sections taken along x (at $z = 2.35$ cm) from the 2D images shown in (a), (b), and (c), respectively.

intensities themselves, which cannot be arbitrarily changed. While the output state of the current system is continuously tunable without collapsing via the parameters $\Delta\Phi_1$ and I_c, the frequency detunings cannot be largely varied due to the small spectral width that EIT operates in and the steep variance of the refractive index within the spectral window.

Another novel feature of this system is that for the out-of-phase case, the two signal beams do not spatially deflect away; instead, due to the attractive central potential induced by the coupling beam, both beams are guided tightly along the central axis, while the axis itself remains dark due to destructive interference. This opens the room for generating dark vortices with an enhanced depth. This feature is possible because in this system, the strength of the attraction is controlled externally by the frequency detuning and intensity of the coupling beam, not by the intensities of the signal fields themselves.

For large two-photon detunings ($\Delta\nu_2 = \pm 250$ MHz) the effect of EIT disappears and the transmission of the resonant probe beams through the vapor cell decreases sharply. In this case, we imaged the incoherent fluorescence signal through one side of the vapor cell. In order to increase the fluorescence signal for imaging, the probe beam's powers were increased to 400 μW each. Even in these large-detuned cases, the spatially varying refractive index due to I_c presents itself as an attractive or a repulsive potential acting on the weak probe fields. The paths of the two resonant probe beams in the absence of the coupling beam are shown in the image taken by CCD1 in Fig. 4(a). The beams look overlapped because in the region between them, the intensities due to the fluorescence caused by each beam add up. For a positive (negative) $\Delta\nu_1$, a positive (negative) $\Delta\nu_2$ pulls both probe beams towards the waveguide center [Fig. 4(b)] while a negative (positive) $\Delta\nu_2$ pushes the weak beams further apart [Fig. 4(c)]. The transverse cross sections of these images at a fixed longitudinal position are shown in Fig. 4(d). While the enhancement and decrease of the resultant intensity in the central axis are apparent from these images and traces, the contrast is degraded due to the large frequency detuning and thus weaker atomic coherence, and also due to background scattering by the windows of the vapor cell. On the other hand, this noise would have been overwhelming had we used the lambda-type atomic configuration, since in that case the strong coupling beam also has access to the ground-state atoms and causes single resonance fluorescence. The signal-to-noise ratio for the fluorescence image is much higher in this three-level ladder-type atomic configuration. In the off-resonance case, while the paths of the spatially displaced weak beams and the resulting fluorescence distribution are unaltered by the relative phase, they respond to the frequency detuning. In the near-EIT-resonance case, both frequency detuning and relative phase significantly influence the two-beam interaction. Interpreting such rich physical mechanisms for the near-EIT resonance case requires a more sophisticated model, which is under construction.

While the current system shares a common capability with a traditional beam splitter, i.e., the combination of two

fields with a phase-dependent output, the current system has some novel features. The first is the combination geometry—this system combines two collinear and nonoverlapping beams by using all-optical cross-Kerr nonlinearity. Second, while the mechanism of beam combination in a traditional beam splitter has fixed transmission and reflection, the transmission and refraction in the current system are tunable. Third, when the two input beams are in phase, the output intensity in the current system can be varied by tuning the coupling beam's intensity since along with the real part of the refractive index, the imaginary part is also tunable. Because of these novel features, the system can be thought of as an all-optically reconfigurable beam combiner for collinear fields, and the new geometry and transistor-like variable output state can be useful in integrated photonic circuits. The all-optical reconfigurability and the underlying mechanism of quantum coherence also distinguishes this system from other static beam-combining systems that might be composed of, say, lenses and optical fibers. Furthermore, since EIT is a natural test bed for slow light as well as stored light [22–33], it will be useful to extend this system to study quantum memory and quantum logic gates involving two ultraweak fields having phase-dependent transverse spatial interactions.

We have thus utilized quantum coherence induced by a strong coupling beam in a three-level atomic system to observe the spatial interactions between two ultraweak signal beams. In the on-resonance case, where absorption is greatly suppressed due to EIT and the transverse profiles of the transmitted probe beams are measured, phase-dependent interactions are observed showing solitonlike combination and repulsion. In the off-resonance case where incoherent scattering is large, the side-way fluorescence is imaged and the frequency-dependent propagation of the two weak beams along the axial direction are observed. We have shown that the system has a large set of tunable parameters (such as single-photon and two-photon frequency detunings, coupling beam power, relative phase between the probe beams), which allow all-optically tunable waveguiding, combining, switching, and routing of ultraweak beams, as well as controlling interactions between them.

U. K. thanks G. Salamo and S. Singh for their invaluable discussions on experimental imaging and numerical ray-tracing methods. U. K. was supported in part by the Raymond H. Hughes Research Fellowship. M. X. was supported in part by NBRPC (Grants No. 2012CB921804 and No. 2011CBA00205).

*ukhadka@princeton.edu
†mxiao@uark.edu
‡Present address: Frick Laboratory, Princeton University, Princeton, 08544 New Jersey, USA.

[1] J. S. Aitchison, A. M. Weiner, Y. Silberberg, D. E. Leaird, M. K. Oliver, J. L. Jackel, and P. W. E. Smith, Opt. Lett. **16**, 15 (1991).
[2] M. Shalaby and A. Barthelemy, Opt. Lett. **16**, 1472 (1991).
[3] M. Shalaby, F. Reynaud, and A. Barthelemy, Opt. Lett. **17**, 778 (1992).
[4] V. Tikhonenko, J. Christou, and B. Luther-Davies, Phys. Rev. Lett. **76**, 2698 (1996).
[5] M.-F. Shih, M. Segev, and G. Salamo, Phys. Rev. Lett. **78**, 2551 (1997).
[6] H. Meng, G. Salamo, M.-f. Shih, and M. Segev, Opt. Lett. **22**, 448 (1997).
[7] G. I. Stegeman and M. Segev, Science **286**, 1518 (1999).
[8] G. I. Segeman, D. N. Christodoulides, and M. Segev, IEEE J. Sel. Top. Quantum Electron. **6**, 1419 (2000).
[9] *Spatial Solitons*, edited by S. Trillo, and W. E. Torruellas (Springerlink, New York, 2001).
[10] R. Y. Chiao, E. Garmire, and C. H. Townes, Phys. Rev. Lett. **13**, 479 (1964).
[11] P. L. Kelley, Phys. Rev. Lett. **15**, 1005 (1965).
[12] J. E. Bjorkholm and A. Ashkin, Phys. Rev. Lett. **32**, 129 (1974).
[13] Y. Silberberg, Opt. Lett. **15**, 1282 (1990).
[14] Z. Jovanoski, J. Mod. Opt. **48**, 865 (2001).
[15] T. Hong, Phys. Rev. Lett. **90**, 183901 (2003).
[16] Y. Wu and L. Deng, Phys. Rev. Lett. **93**, 143904 (2004).
[17] H. Shpaisman, A. D. Wilson-Gordon, and H. Friedmann, Phys. Rev. A **71**, 043812 (2005).
[18] H. Michinel, M. J. Paz-Alonso, and V. M. Perez-Garcia, Phys. Rev. Lett. **96**, 023903 (2006).
[19] D. D. Yavuz, Phys. Rev. A **75**, 041802(R) (2007).
[20] G. Huang, C. Hang, and L. Deng, Phys. Rev. A **77**, 011803(R) (2008).
[21] H.-J. Li., L. Dong, C. Hang, and G. Huang, Phys. Rev. A **83**, 023816 (2011).
[22] H.-J. Li, Y.-P. Wu, and G. Huang, Phys. Rev. A **84**, 033816 (2011).
[23] M. Xiao, Y.-Q. Li, S.-Z. Jin, and J. Gea-Banacloche, Phys. Rev. Lett. **74**, 666 (1995).
[24] J. Gea-Banacloche, Y.-Q. Li, S.-Z. Jin, and M. Xiao, Phys. Rev. A **51**, 576 (1995).
[25] R. R. Moseley, S. Shepherd, D. J. Fulton, B. D. Sinclair, and M. H. Dunn, Phys. Rev. Lett. **74**, 670 (1995).
[26] L. V. Hau, S. E. Harris, Z. Dutton, and C. H. Behroozi, Nature (London) **397**, 594 (1999).
[27] C. Liu, Z. Dutton, C. H. Behroozi, and L. V. Hau, Nature (London) **409**, 490 (2001).
[28] D. F. Phillips, A. Fleischhauer, A. Mair, R. L. Walsworth, and M. D. Lukin, Phys. Rev. Lett. **86**, 783 (2001).
[29] A. Mair, J. Hager, D. F. Phillips, R. L. Walsworth, and M. D. Lukin, Phys. Rev. A **65**, 031802(R) (2002).
[30] X. L. Song, L. Wang, Z. H. Kang, R. Z. Lin, X. Li, Y. Jiang, and J. Y. Gao, Appl. Phys. Lett. **91**, 071106 (2007).
[31] R. M. Camacho, C. J. Broadbent, I. Ali-Khan, and J. C. Howell, Phys. Rev. Lett. **98**, 043902 (2007).
[32] L. Zhao, T. Wang, Y. Xiao, and S. F. Yelin, Phys. Rev. A **77**, 041802(R) (2008).
[33] G. Hetet, J. J. Longdell, M. J. Sellars, P. K. Lam, and B. C. Buchler, Phys. Rev. Lett. **101**, 203601 (2008).